1   **A pulse-decay method for low permeability analyses of granular rock**

2   **media**

3   Tao Zhang[1], Qinhong Hu[1*], Behzad Ghanbarian[2], Derek Elsworth[3], Zhiming Lu[4]

4   [1] Department of Earth and Environment Sciences, University of Texas at Arlington,

5   Arlington, TX 76019, United States

6   [2] Porous Media Research Lab, Department of Geology, Kansas State University, Manhattan,

7   KS 66506, United States

8   [3] Department of Energy and Mineral Engineering, G3 Centre and Energy Institute, The

9   Pennsylvania State University, University Park, PA 16802, United States

10   [4] The Earth and Environmental Sciences Division, Los Alamos National Laboratory, Los

11   Alamos, NM 87544, United States

12

13

14

15

16

17

18

19

20

21   *** Corresponding author:** maxhu@uta.edu

22   **Abstract:** Nano-darcy level permeability measurements of porous media,

23   such as nano-porous mudrocks, are only practically feasible with gas invasion

24   methods into granular-sized samples with short diffusion lengths and thereby

25   reduced experimental duration; however, these methods lack rigorous

26   solutions and standardized experimental procedures. For the first time, we

27   resolve this by providing an integrated technique (termed as gas permeability

28   technique) with coupled theoretical development, experimental procedures,

29   and data interpretation workflow. Three exact mathematical solutions for

30   transient and slightly compressible spherical flow, along with their asymptotic

31   solutions, are developed for early- and late-time responses. Critically, one late-

32   time solution is for an ultra-small gas-invadable volume, important for a wide

33   range of practical usages. Developed as applicable to different sample

34   characteristics (permeability, porosity, and mass) in relation to the storage

35   capacity of experimental systems, these three solutions are evaluated from

36   essential considerations of error difference between exact and approximate

37   solutions, optimal experimental conditions, and experimental demonstration

38   of mudstone and molecular-sieve samples. Moreover, a practical workflow of

39   solution selection and data reduction to determine permeability is presented

40   by considering samples with different permeability and porosity under various

41   granular sizes. Overall, this work establishes a rigorous, theory-based, rapid,

42   and versatile gas permeability measurement technique for tight media at sub-

43   nano darcy levels.

44   **Keywords:** permeability; granular samples; pulse-decay; mathematical

45   solutions; experimental methods.

46   **Highlights:**

47   • An integrated (both theory and experiments) gas permeability
48   technique (GPT) is presented.

49   • Exact and approximate solutions for three cases are developed with
50   error discussion.

51   • Conditions of each mathematical solution are highlighted for critical
52   parameters.

53   • Essential experimental methodologies and data processing procedures
54   are provided and evaluated.

1. Introduction

Shales, crystalline, and salt rocks with low permeabilities (e.g., $<10^{-17}$ m^2 or 10 micro-darcies µD) are critical components to numerous subsurface studies. Notable examples are the remediation of contaminated sites(Neuzil, 1986; Yang et al., 2015), long-term performance of high-level nuclear waste repositories (Kim et al., 2011; Neuzil, 2013), enhanced geothermal systems (Huenges, 2016; Zhang et al., 2021), efficient development of unconventional oil and gas resources (Hu et al., 2015; Javadpour, 2009), long-term sealing for carbon utilization and storage (Fakher et al., 2020; Khosrokhavar, 2016), and high-volume and effective gas (hydrogen) storage (Liu et al., 2015; Tarkowski, 2019). For fractured rocks, the accurate characterization of rock matrix and its permeability is also critical for evaluating the effectiveness of low-permeability media, particularly when transport is dominated by slow processes like diffusion (Ghanbarian et al., 2016; Hu et al., 2012).

Standard permeability test procedures in both steady-state and pulse-decay methods use consolidated core-plug samples (e.g., 2.54 cm in diameter), which may contain fractures and show dual- or triple-porosity characteristics (Abdassah and Ershaghi, 1986; Bibby, 1981). The overall permeability may therefore be controlled by a few bedding-oriented or cross-cutting fractures, even if experiments are conducted at reservoir pressures (Bock et al., 2010;

75   Gensterblum et al., 2015; Gutierrez et al., 2000; Luffel et al., 1993). Fractures

76   might be naturally- or artificially-induced (e.g., created during sample

77   processing), which makes a comparison of permeability results among

78   different samples difficult (Heller et al., 2014). Hence, methods for measuring

79   the matrix (non-fractured) permeability in tight media, with a practical

80   necessity of using granular samples, have attracted much attention to eliminate

81   the confounding effect of fractures (Civan et al., 2013; Egermann et al., 2005;

82   Heller et al., 2014; Wu et al., 2020; Zhang et al., 2020).

83   A GRI (Gas Research Institute) method was developed by Luffel et al. (1993)

84   and followed by Guidry et al. (1996) to measure the matrix permeability of

85   crushed mudrocks (Guidry et al., 1996; Luffel et al., 1993). Such a method

86   makes permeability measurement feasible in tight and ultra-tight rocks (with

87   permeability $< 10^{-20}$ m^2 or 10 nano-dcarcies, nD), particularly when

88   permeability is close to the detection limit of the pulse-decay approach on core

89   plugs at ~10 nD (e.g., using commercial instrument of PoroPDP-200 of

90   CoreLab). In the GRI method, helium may be used as the testing fluid to

91   determine permeability on crushed samples at different sample sizes (e.g.,

92   within the 10-60 mesh range). The limited mesh size of 20-35 (500-841 μm in

93   diameter) was recommended in earlier works, which has led to the colloquial

94   names of "the GRI method/size" in the literature (Cui et al., 2009; Kim et al.,

95   2015; Peng and Loucks, 2016; Profice et al., 2012). However, Luffel et al.

96   (Guidry et al., 1996; Luffel et al., 1993) did not document the processing

97   methodologies needed to derive the permeability from experimental data from

98   such a GRI method. That is, there are neither standard experimental

99   procedures for interpreting gas pulse-decay data in crushed rock samples nor

100   detailed mathematical solutions available for data processing in the literature

101   (Kim et al., 2015; Peng and Loucks, 2016; Profice et al., 2012). In this work,

102   we achieve to: (1) develop mathematical solutions to interpret gas pulse-decay

103   data in crushed rock samples without published algorithm available as this

104   method shares different constitutive phenomena to the traditional pulse-decay

105   method for core plug samples in Cartesian coordinates; and (2) present

106   associated experimental methodology to measure permeability, reliably and

107   reproducibly, in tight and ultra-tight granular media.

108   The rest of this article is organized as follows. We first derive the

109   constitutive equations for gas transport in granular (unconsolidated or crushed

110   rock) samples. Specifically, we develop three mathematical solutions which

111   cover different experimental situations and sample properties. As each

112   solution shows its own pros and cons, we then in detail present the error

113   analyses for the derived exact and approximate solutions and discuss their

114   applicable requirements and parameter recommendation for practical usages.

115   This work aims to fill the knowledge gap of the granular rock (matrix)

116   permeability measurement and follow-on literature by establishing an

117   integrated methodology for reproducible measurements of nD-level

118   permeability in tight rock for emerging energy and resources subsurface

119   studies.

120   **2. Mathematical solutions for gas permeability of granular samples**

121   For a compressible fluid under unsteady-state conditions, flow in a porous

122   medium can be expressed by the mass conservation equation:

123    $$\frac{\partial p}{\partial t} + \nabla \cdot (\rho \overline{v}) = 0 \qquad (1A)$$

124   where p is the pressure, t is the time, ρ is the fluid density, and $\overline{v}$ is the

125   Darcy velocity. In continuity equations derived for gas flow in porous media,

126   permeability can be treated as a function of pressure through the ideal gas law.

127   Constitutive equations are commonly established for a small pressure

128   variation to avoid the non-linearity of gas (the liquid density to be a constant)

129   and to ensure that pressure would be the only unknown parameter (Haskett et

130   al., 1988). For spherical coordinates of fluid flow in porous media, assuming

131   flow along the radial direction of each spherical solid grain, Eq. (1A) becomes

132    $$\frac{\partial p}{\partial t} \phi = \frac{1}{c_t} \frac{k}{\mu r^2} \frac{\partial}{\partial r} \left(r^2 \frac{\partial p}{\partial r} \right) \qquad (1B)$$

133   The gas compressibility c_t is given by

134
$$c_t = \frac{1}{\rho}\frac{d\rho}{dp} = \frac{1}{p} - \frac{1}{z}\frac{dz}{dp} \qquad (1C)$$

135   In Eqs. (1B) and (1C), ϕ and k are sample porosity and permeability, r

136   is the migration distance of fluid, μ is the fluid viscosity, and z is the gas

137   deviation (compressibility) factor and is constant.

138   To correct for the non-ideality of the probing gas, we treat gas density as a

139   function of pressure and establish a relationship between the density and the

140   permeability through a pseudo-pressure variable (given in the 1st part of

141   Supplemental Information SI1). Detailed steps for deriving mathematical

142   solutions for the GPT can be found in SI2, based on heat transfer studies

143   (Carslaw and Jaeger, 1959). The Laplace transform, in combination with the

144   Bessel equation, is an efficient tool for solving gas transport in granular

145   samples with low permeabilities, as applied in this study. Alternatively, other

146   approaches, such as the Fourier analysis, Sturm-Liouville method, or Volterra

147   integral equation of the second form may be used (Carslaw and Jaeger, 1959;

148   Haggerty and Gorelick, 1995; Ruthven, 1984).

149   We applied dimensional variables to derive the constitutive equation given

150   in Eq. **Error! Reference source not found.** for which the initial and

151   boundary conditions are

152
$$\frac{\partial^2 U_s}{\partial \xi^2} + s^2 U_s = 0 \bigg|_{U_s=0,\xi=0} \qquad (1D)$$

153
$$\alpha^2(U_s - 1) = \frac{3}{K_c}\left(\frac{\partial U_s}{\partial \xi} - \frac{U_s}{\xi}\right)\Big|_{\xi=1} \qquad (1E)$$

154 where U_s and ξ represent the dimensionless values of gas density and

155 sample scale, and s is the transformed Heaviside operator. α in Eq. (2B) is

156 determined by solving Eq. (S30) for its root. K_c in Eq. (1E) is a critical

157 parameter that represents the volumetric ratio of the total void volume of the

158 sample cell to the pore volume of the porous samples. It is similar to the

159 storage capacity, controlling the acceptable measurement range of

160 permeability and decay time, in the pulse-decay method proposed by Brace et

161 al. in 1986 (Brace et al., 1968).

162   The fractional gas transfer for the internal (limited K_c value) and external

163 (infinite K_c value) gas transfer of sample is given by

164
$$F_f = 1 - 6\sum_{n=1}^{\infty}\frac{K_c(1+K_c)e^{-\alpha n^2 \tau}}{9(K_c+1)+\alpha_n^2 K_c^2} \qquad (1F)$$

165
$$F_s = 1 - \frac{6}{\pi^2}\sum_{n=1}^{\infty}\frac{e^{-(n\pi)^2 \tau}}{n^2} \qquad (1G)$$

166 where F_f and F_s represent the uptake rate of gas outside and inside the

167 sample separately as a dimensionless parameter, and τ is the Fourier number

168 of dimensionless time. Three approximate solutions of the transport

169 coefficient based on Eqs. (2C) and (2D) for various conditions are presented

170   below.

171   The late-time solution to Eq. (1F) for a limited K_c value (called LLT

172   hereafter) is

$$k = \frac{R_a{}^2 \mu c_t \phi_f s_1}{\alpha_1{}^2} \qquad (3A)$$

173

174   The late-time solution to Eq. (1G) when K_c tends to infinity (ILT hereafter)
175   is

$$k = \frac{R_a{}^2 \mu c_t \phi_f s_2}{\pi^2} \qquad (3B)$$

176

177   The early-time solution to Eq. (1G) when K_c approaches infinity (IET
178   hereafter) is

$$k = \frac{\pi R_a{}^2 \mu c_t \phi_f s_3}{36} \qquad (3C)$$

179

180   In Eq. (3), R_a is the particle diameter of a sample, and s_1, s_2, and s_3 are

181   the three exponents that may be determined from the slopes of data on double

182   logarithmic plots. Table 1 summarizes Eqs. (3A) to (3C) and conditions under

183   which such approximate solutions would be valid.

184   Table 1. Solutions schematic with difference K_c and τ values

Parameter	Symbol	Remarks		
Volume fraction[§]	K_c	Limited value for $K_c < 10$		Infinity value for $K_c > 10$
Exact. Density fraction[£]	F	F_f		F_s
Approx. Solution of Density fraction[*]	Eqs. (3A-3B)	Eq. (3A) (LLT)	Eq. (3C) (IET)	Eq. (3B)) (ILT)
Available Dimensionless time for Approx. solution	τ	Late-time solution $\tau > 0.024$	Early-time solution $\tau < 0.024$	Late-time solution $\tau > 0.024$

[§] It defines as the volumetric ratio of the total void volume of the sample cell to the pore volume of the porous samples, the classification between the limited and infinity value is proposed as 50 with the following analyses.
[£] The original constitutive equation for different K_c value.
[*] Eqs. (3A-3C) are three approximate solutions of density faction function F.

185   Based on diffusion phenomenology, Cui et al. (2009) presented two

186   mathematical solutions similar to our Eqs. (3A) and (3C). In the work of Cui

187   et al. (2009), however, the lack of detailed analyses of τ and K_c in the

188   constitutive equations may deter the practical application of Eq. (3B), which

189   is unable to cover an experimental condition of small sample mass with a

190   greater τ (further analyzed in section 3). In addition to that, Cui et al. (2009)

191   did not comprehensively assess practical applications of their two solutions,

192   which is addressed in this study. Hereafter, we refer to the developed

193   mathematical and experimental, gas-permeability-measurement approach

194   holistically as gas permeability technique (GPT).

195   **3. Practical usages of algorithms for the GPT**

196   As aforementioned, mathematical solutions given in Eqs. (3A) and (3B)

197   were deduced based on different values of K_c and τ as shown in the SI2.

198   This means each solution hold only under specific experimental conditions,

199   which are mostly determined by the permeability, porosity, and mass of

200   samples, as well as gas pressure and void volume of the sample cell. In this

201   section, the influence of parameters K_c and τ on the solution of constitutive

202   equation is analyzed and a specific value of dimensionless time ($\tau = 0.024$) is

203   proposed as the criterion required to detect the early-time regime from the late-

204   time one for the first time in the literature. We also demonstrate that the early-

205   time solution of Eq. (3C), which has been less considered for practical

206   applications in previous studies, is also suitable and unique under common

207   situations. Besides, the error of the approximate solution compared to the

208   exact solution and their capabilities are discussed, as it helps select an

209   appropriate mathematical solution at small τ values. Moreover, we showcase

210   the unique applicability and feasibility of the new solution of Eq. (3B).

211   **3.1 Sensitivity analyses of the K_c value for data quality control**

212   To apply the GPT method, appropriately selecting the parameter K_c in Eqs.

213   (3A)-(3C) is crucial, as it is a critical value for data quality control. Recall that

214   K_c represents the volumetric ratio of the total void volume of the sample cell

215   to the pore volume of the porous samples. The dimensionless density outside

216   the sample, U_f, is related to K_c via Eq. (S33) in the SI2. One may simplify

217   Eq. (S33) by replacing the series term with some finite positive value and set

218    $$U_f - \frac{K_c}{1+K_c} > 0 \qquad (1K)$$

219   We define $K_f = K_c/(1 + K_c)$ to interpret the density variance of the system

220   as K_f is closely related to the dimensionless density outside the sample, U_f.

221   Eq. (1K) shows the relationship between the U_f and K_c (plotted in Fig.

222   1). For $K_c > 0$, K_f falls between 0 and 1. The greater the K_f value is, the

223   insensitive to density changes the system would be. For K_c equal to 50 (not

224   shown in Fig. 1), K_f would no longer be sensitive to K_c variations as it has

225   already approached 98% of the dimensionless density. This means that the U_f

226   value needs to be greater than 0.98, and this leaves only 2% of the fractional

227   value of U_f available for capturing gas density change. When K_c is 100, the

228   left fractional value of U_f would be 1%. This would limit the amount of data

229   available (the linear range in Fig. S1) for the permeability calculation, which

230   would complicate the data processing. Thus, for the GPT experiments, a small

231   value of K_c (less than 10) is recommended, as K_f nearly reaches its plateau

232   beyond $K_c = 10$ (Fig. 1). When K_c is 10, the left fractional value of U_f is

233   only as low as 9%.
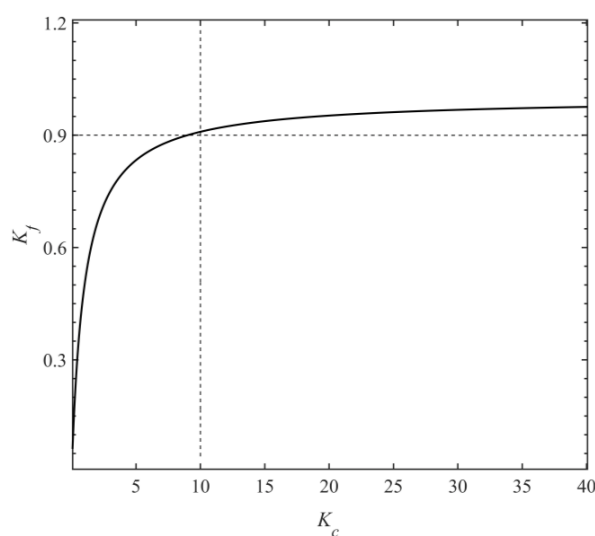
234

235   Fig. 1. Dimensionless density, K_f, as a function of dimensionless volume K_c.

236   Recall that $K_f = K_c/(1 + K_c)$. Major variations in K_f occur for $K_c < 10$ indicating

13

237   longer gas transmission duration with more pressure-decay data available for

238   permeability derivation.

239

240   **3.2 Recommendation for solution selection**

241   The following three aspects need to be considered before selecting the

242   appropriate solution for permeability calculation: 1) selecting early- or late-

243   time solutions; 2) error between the approximate and exact solutions; and 3)

244   the convenience and applicability of solutions suitable for different

245   experiments. We will first discuss the selection criteria for early- or late-time

246   solutions.

247   Fig. 2(a) shows the exact solution of F_s with their two approximate early-

248   and late-time solution (Table 1). Two exact solutions of F_f for K_c equals to

249   10, 50 are also demonstrated in Fig. 2(a). Fig. 2(b) depicts the exact solution

250   from F_f for different K_c values from 1 to 100 and their corresponding

251   approximate solution for Eq. (3A). The intersection point of the solution Eq.

252   (3B) and Eq. (3C), namely $\tau = 0.024$ in Fig. 2(a), is used for distinguishing

253   early- and late-time solutions.

254   Two notable observations can be drawn from Fig. 2(b). Firstly, the

255   approximate solution Eq. (3A) would only be applicable at late times when

256   τ is longer than 0.024. For $\tau < 0.024$, regardless of the K_c value, Eq. (3C)

14

257 would be more precise than Eqs. (3A) and (3B) and return results close to the

258 exact solution for both F_f and F_s. Secondly, results of Eqs. (3A) and (3B)

259 presented in Fig. 2(a) are similar; there is only a minor difference but become

260 very close at greater K_c values especially for $K_c > 10$. Due to the fact that

261 core samples from deep wells are relatively short in length and their void

262 volume is small (ultra-low porosity and permeability such as in mudstones

263 with $k \leq 0.1$ nD), in practice, a solution for $10 < K_c < 100$ is the most

264 common outcome, even if the sample cell is loaded as full as possible. Under

265 such circumstances, the newly derived solution, Eq. (3B), becomes practical

266 and convenient: 1) if the K_c and dimensionless time τ have not been

267 evaluated precisely before the GPT experiment, this solution may fit most

268 experimental situations; 2) this solution is suitable for calculation as it does

269 not need the solution from the transcendental equation of Eq. (S30) because

270 the denominator of α has been replaced by π. The data quality control is

271 discussed in Section 4.1.
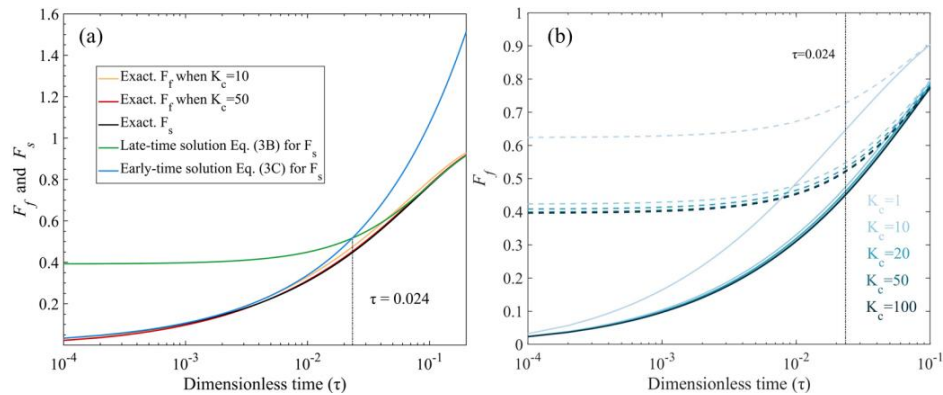
Fig. 2. Three GPT solutions with different values of τ, K_c; the dashed lines are approximate solutions without a series expansion in Fig. (2b) for F_f. Figure modified from Cui et al. (2009).

3.3 Applicability of the early-time solution

A small K_c value can guarantee a sufficient time for gas transfer in samples and provide enough linear data for fitting purposes. We note that the selection of the limited K_c solution of F_f, and the infinity K_c solution F_s is controlled by K_c. However, before the selection of K_c, the dimensionless time is the basic parameter to be estimated as a priori before the early- or late-time solutions are selected.

For pulse-decay methods, the early-time solution has the advantage of capturing the anisotropic information contained in reservoir rocks (Jia et al., 2019; Kamath, 1992). However, it suffers from the shortcoming of uncertainty

16

286   in data for initial several seconds, which as a result is not recommended for

287   data processing (Jia et al., 2019; Kamath, 1992). This is due to: (1) the Joule-

288   Thompson effect, which causes a decrease in gas temperature from the

289   expansion; (2) kinetic energy loss during adiabatic expansion; and (3) collision

290   between molecules and the container wall. These uncertainties normally

291   happen in the first 10-30 sec, shown in our experiments as a fluctuating period

292   called "Early Stage".

293   However, the "Early Stage" present in pulse-decay experiments does not

294   mean that the early-time solution is not applicable. We demonstrate the

295   relationship between time and dimensionless time in Fig. 3 that a short

296   dimensionless time may correspond to a long testing period of hundred to

297   thousand seconds in experiments. For example, ultra-low permeability

298   samples with $k \leq 0.1$ nD and small dimensionless times $\tau < 0.024$. This

299   situation would only be applicable to early-time solution, but with data

300   available beyond the "Early Stage" and provide available data in a long time

301   (hundreds to thousands of seconds). For example, the early-time solution

302   would fit ultra-low permeability samples in 600s around for 0.1 nD, and at

303   least 1000s for 0.01 nD shown in Fig. 3 in the region below the dark line. Then,

304   using Eq. (3C), the derived permeability would be closer to its exact solution

305   in the earlier testing time (but still after the "Early Stage"). For mudrock

306   samples that we have tested (results presented in Section 5.3), permeabilities

307   are low and in the order of 0.1 nD.
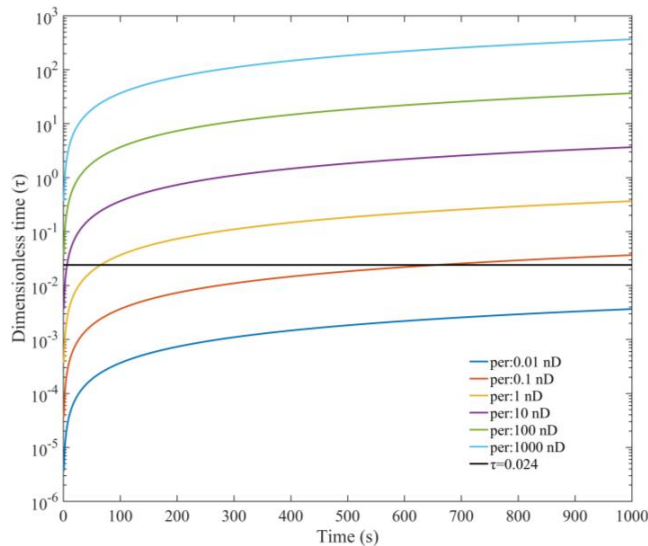
308

309   Fig. 3 Dimensionless time τ versus actual times for different permeability values

310   trough Eq. (S14) using He gas, sample porosity of 5%, and sample diameter of 2

311   mm.

312   **3.4 Error analyses between exact and approximate solutions**

313   It is unpractical to use the exact solutions with their series part to do the

314   permeability calculation; thus, only the approximate solutions are used and the

315   error difference between the exact and approximate solutions is discussed here.

18

316 The original mathematical solutions, Eqs. (S39) and (S49), are based on

317 series expansion. For dimensionless densities F_f and F_s in Eqs. (S39) and

318 (S49), their series expansion terms should converge. However, the rate of

319 convergence is closely related to the value of τ. For example, from Eq. (S30),

320 when $\tau \geq 1$, the exponent parts of U_s and U_f are at least $(2n + 1)\pi^2$.

321 Therefore, the entire series expansion term can be omitted without being

322 influenced by K_c. In practical applications, the solutions given in Eqs. (3A)-

323 (3C) are approximates without series expansion. In this study, we provide the

324 diagrams of change in errors with dimensionless time in the presence of

325 adsorption (Fig. 4).

326 For F_f, the error differences between the exact and approximate solutions

327 are 3.5% and 0.37% for τ=0.05 and 0.1 when K_c=10, respectively. When $\tau \leq$

328 0.024, the error would be greater than 14.7%. Fig. 2(b) shows that F_f can be

329 approximated as F_s when K_c is greater than 10; the error difference between

330 F_f and F_s is quite small at this K_c value (for K_c=10, 6.6% is the maximum

331 error when τ=0.01; 4.4% when τ=0.05; and 2.9% when τ=0.1) as shown in

332 Fig. 4.

333 For F_s, the error difference is roughly the same as F_f and equal to 3.6%

334 for $\tau = 0.05$ and 0.38% for $\tau = 0.1$. This verifies that new derived Eq. (3B)

335 is equivalent to Eq. (3A) when K_c is greater than 10. As for the evaluation

336 of Eq. (3C), the error difference with the exact solution will increase with

337 dimensionless time (5.1% for $\tau = 0.003$, 9.7% for $\tau = 0.01$, and 16% for $\tau =$

338 0.024).
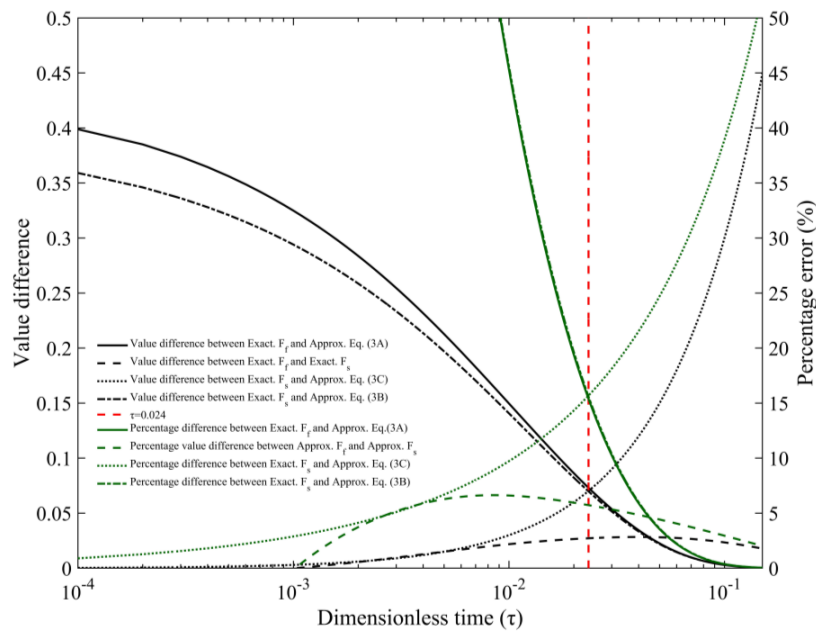
339

340 Fig. 4. Error analyses of F_f and F_s for their exact and approximate solutions

341 In the following, we apply the approximate solutions, Eqs. (3A-3C), to

342 some detailed experimental data and determine permeability in several shale

343 samples practically compatible with sample size, gases, and molecular

344 dynamics analyses.

345 **4. Influence of kinetic energy on gas transport behavior**

346 **4.1 Flow state of gas in granular samples**

347   During the GPT, with the boundary conditions described in SI2, the pressure

348   variation is captured after gas starts to permeate into the sample from the edge,

349   and the model does not take into account the gas transport between particles

350   or into any micro-fractures, if available. Thus, the transport that conforms to

351   the "unipore" model and occurs after the "Early Stage" (defined in Section 3.3)

352   and or during the "Penetration Zone" (the area between the two vertical lines

353   in Fig. 5), should be used to determine the slope. See Fig. S2 in which it is

354   shown how to obtain the permeability result using the applicable mathematical

355   solutions (Eqs. 3A-C). Fig. 5 shows the pressure variance with time during the

356   experiment using different sample size from sample X-1. Similar pattern was

357   observed for sample X-2 as well. From Fig. 5, the time needed to reach

358   pressure equilibrium after the initial fluctuation stage is 20-100 sec, and the

359   Penetration Zone decreases with decreasing grain size over this time period.

360
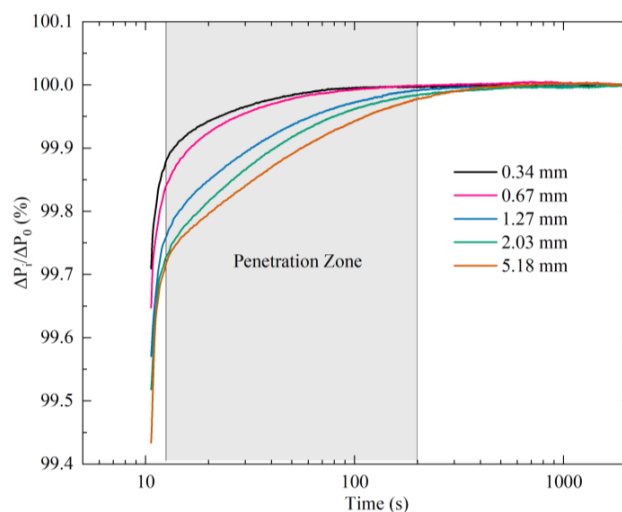
Fig. 5. Fitting region (the "Penetration Zone" in the shadowed area) for mudrock

sample X-1 with different granular sizes; the penetration zone illustrating the

pressure gradient mainly happens at 20 to 200 sec for this sample.

In fact, the "Penetration Zone", as an empirical period, is evaluated by the

pressure change over a unit of time before gas is completely transported into

the inner central part of the sample to reach the final pressure. Owing to the

sample size limitation, a decreasing pressure could cause multiple flow states

(based on the Knudsen number) to exist in the experiment. The pressure during

the GPT experiment varies between 50 and 200 psi. Fig. 6 shows the Knudsen

number calculated from different pressure conditions and pore diameters

together with their potential flow state. Based on Fig. 6, the flow state of gas

in the GPT experiments is mainly dominated by Fickian and transition

22

374   diffusion. Essentially, the flow state change with pressure should be strictly

375   evaluated through the Knudsen number in Fig. 6 to guarantee that the data in

376   the "Penetration Zone" are always fitted with the GPT's constitutive equation

377   for laminar or diffusive states. This helps obtain a linear trend for $ln(1-$

378     $F_f)$ or F_s^2 versus time for low-permeability media. Experimentally, data from

379   30 to several 100 seconds are recommended for tight rocks like shales within

380   the GPT methodology.
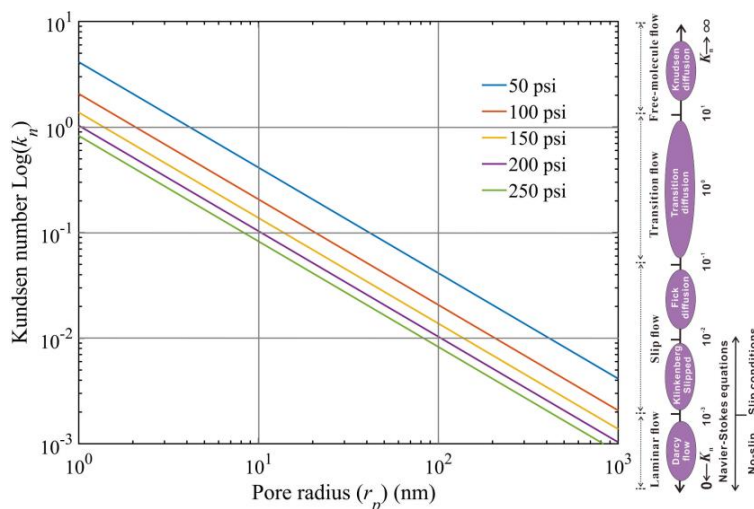
381

382   Fig. 6. Flow state of gas under diffferent testing pressures; modified from Chen &

383   Pfender (1983) and Roy et al. (2003) (Chen and Pfender, 1983; Roy et al.,

384   2003).

385

386   In the GPT approach, as mentioned earlier, Eq. (S33) holds for small K_c

387   values (e.g., < 10) so that the approximately equivalent void volume in the

388   sample cell and sample pore volume would allow for sufficient pressure drop.

389   It also gives time and allows the probing gas to expand into the matrix pores

390   to have a valid "Penetration Zone" and to determine the permeability. Greater

391   values of K_c would prevent the gas flow from entering into a slippage state

392   as the pressure difference would increase with increasing K_c. However, large

393   pressure changes would result in a turbulent flow (Fig. 6), which would cause

394   the flow state of gas to be no longer valid for the constitutive equation of the

395   GPT. Overall, the GPT solutions would be applicable to the gas permeability

396   measurement, based on the diffusion-like process, from laminar flow to

397   Fickian diffusion, after the correction of the slippage effect. Though the liquid

398   permeability is not complicated by the gas slippage effect, the liquid test is

399   difficult in achieving the flow state of Knudsen number greater than 10^{-3},

400   which normally occurs in the ultra-low permeability media. Therefore, gases

401   are chosen, and practically needed, as the testing fluid in this work.

4.2 Pressure decay behavior of four different probing gases

403   We used three inert gases, including He, N_2, and Ar, and one sorptive gas

404   i.e., CO_2 (Busch et al., 2008), to compare the pressure drop behavior for

405   sample size of 0.675 mm (average granular diameter). Results for the mudrock

406   sample X-2 are presented in Fig. 7. Among the three inert gases, helium and

407 argon required the shortest and longest time to reach pressure equilibrium (i.e.,

408 He<N_2<Ar). For pressure range, argon had the greatest pressure drop. In a

409 constant-temperature system, the speed (or rate) at which gas molecules move

410 is inversely proportional to the square root of their molar masses. Hence, it is

411 reasonable that helium (with the smallest kinetic diameter of 0.21 nm) has the

412 shortest equilibrium time. However, the pressure drop is more critical than the

413 time needed to reach equilibrium for the GPT, as the equilibrium time does not

414 differ much (basically within 10 seconds for a given sample weight, except for

415 the adsorptive CO_2). Argon may provide a wider range of valid Penetration

416 Zones in a short time scale for its longest decay time except for adsorbed gas

417 of CO_2; a choice of inert and economical gas is suggested for the GPT

418 experiments.
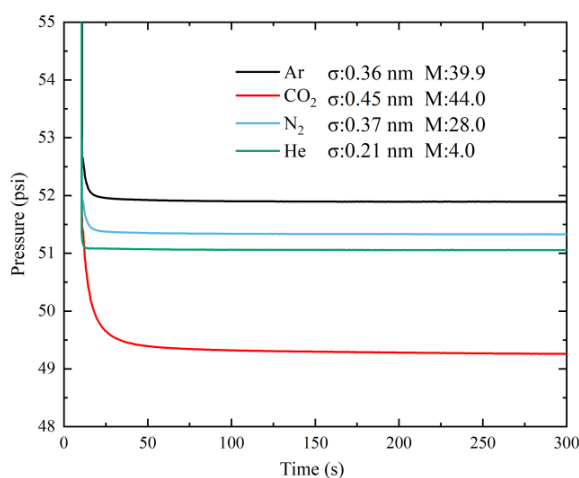
419

420 Fig. 7. Measured pressure decay curves from mudrock Sample X-2 for gases of

421   different molecular diameters σ and molecular weights M (g/mol).

422

423   Fig. 7 shows that the pressure decay curve of the adsorptive gas CO_2 is

424   different from those of the inert gases used in this study. CO_2 has a slow

425   equilibrium time due to its large molar mass, and the greatest pressure drop

426   among the four gases due to its adsorption effect. This additional flux needs to

427   be taken into account to obtain an accurate transport coefficient. Adsorption

428   of CO_2 is stronger than that of CH_4, especially in micropores in tight reservoirs

429   (Busch et al., 2008). Accordingly, multiple studies including laboratory

430   experiments (Pini, 2014) and long-term field observations (Haszeldine et al.,

431   2006; Lu et al., 2009) were carried out to assess the sealing efficiency of

432   mudrocks for CO_2 storage. In fact, the GPT can supply a quick and effective

433   way to identify the adsorption behavior of different mudrocks for both

434   laminar-flow and diffusion states.

435   **4.3 Pressure decay behavior for different granular sizes**

436   We compared the pressure drop behavior of gas in the mudstone Sample X-

437   1 with different granular sizes (averaged from 0.34 mm to 5.18 mm) using the

438   same sample weight and K_c. Results based on the experimental data shown in

439   Fig. 8 indicate that a larger-sized sample would provide more analyzable data

440   to determine the permeability. This because the larger the granular size, (1) the

441   larger the pressure drop, (2) the longer the decay time as Fig. 8 demonstrates.

442   The is consistent with the simulated results reported by Profice et al. (2012)

443   (Profice et al., 2012).
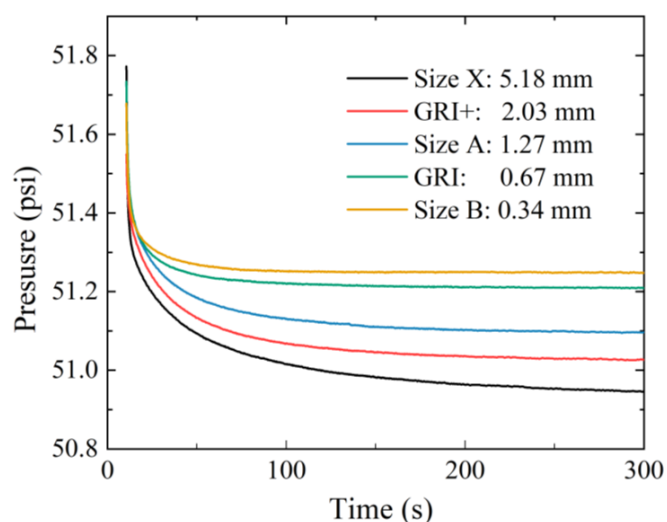
444

445   Fig. 8. Pressure decay curves measured by helium on sample X-1 with five different

446   granular sizes. The intra-granular porosity was 5.8% independently measured by

447   mercury intrusion porosimetry.

448

449   Table 2. Permeability results from the methods of GPT and SMP-200 for X-1.

Size (mm)	SMP-200 (nD) §	GPT test 1 (nD)£	GPT test 2 (nD)£	Average value (nD)£	Fitting duration (s)	Solution type	Dimensionless time	Particle density (g/cm³)
5.18	-	1.17	1.17	1.17	50-100	ILT	0.023-0.027	2.631
2.03	14.2	0.45	0.41	0.43	50-100	LLT	0.026-0.028	2.626
1.27	-	0.10	0.10	0.10	30-60	ILT	CR*	2.673
0.67	0.65	0.08	0.04	0.06	30-60	LLT	CR*	2.658
0.34	-	0.02	-	0.02	30-60	IET	CR*	2.643

§ The results are from the SMP-200 using the GRI default method.

£ The results are from the GPT method we proposed.

* CR means the conflict results that the verified dimensionless time does not confirm the early- or late-time solutions using the
solved permeability. For example, the verified dimensionless time would be > 0.024 using the early-time solution solved result and

27

vice versa.

450   As reported in Table 2, the permeability values measured by the GPT

451   method are one or two orders of magnitude greater than those measured by the

452   SMP-200 instrument. The built-in functions of SMP-200 can only be used for

453   two default granular sizes (500-841 μm for GRI and 1.70-2.38 mm for what

454   we call GRI+) to manually curve-fit the pressure decay data and determine the

455   permeability. The GRI method built in the SMP-200 only suggests the fitting

456   procedure for data processing without publicly available details of underlying

457   mathematics. The intra-granular permeabilities of mudrock sample X-1 vary

458   from 0.02 to 1.17 nD for five different granular sizes using the GPT. With the

459   same pressure decay data selected from 30 to 200 sec, the permeability results

460   for GRI and GRI+ sample sizes from the SMP-200 fitting are 0.65 and 14.2

461   nD, as compared to 0.06 and 0.43 nD determined by the GPT using the same

462   mean granular size. Our results are consistent with those reported by Peng &

463   Loucks (2016) who found two to three orders of magnitude differences

464   between the GPT and SMP-200 methods (Peng and Loucks, 2016).

465   There exist several issues associated with granular samples with

466   diameters smaller than Size A (average diameter of 1.27 mm). First, the testing

467   duration is short, and second, there would not be sufficient pressure variation

468   analyzed in Fig. 8. Both may cause significant uncertainties in the

469   permeability calculation and, therefore, make samples with diameters smaller

470   than Size A unfavorable for the GPT method, particularly extra-tight (sub-nD

471   levels) samples, as there is almost no laminar or diffusion flow state to be

472   captured. The greater pressure drop for larger-sized granular samples would

473   result in greater pressure variation and wider data region compared to smaller

474   granular sizes (see Figs. 6 and 9). Although samples of large granular sizes

475   may potentially contain micro-fractures, which complicate the determination

476   of true matrix permeability (Heller et al., 2014), the versatile GPT method can

477   still provide size-dependent permeabilities for a wide range of samples (e.g.,

478   from sub-mm to 10 cm diameter full-size cores) (Ghanbarian, 2022a, b).

479   Besides, the surface roughness of large grains may also complicate the

480   determination of permeability, which need to pay attention to (Devegowda,

481   2015; Rasmuson, 1985; Ruthven and Loughlin, 1971). Overall, our results

482   demonstrated that sample diameters larger 2 mm are recommended for the

483   GPT to determine the nD permeability of tight mudrocks or crystalline rocks,

484   while smaller sample sizes may produce uncertain results.

485   **4.4 Practical recommendations for the holistic GPT**

486   Here, we evaluate the potential approximate solution for tight rock

487   samples using frequently applied experimental settings by considering the

488   critical parameters, such as sample mass, porosity, and estimated permeability

29

489   (as compiled in Fig. 9 showing the dimensionless time versus porosity). Based

490   on the results presented in Figs. 3 and 6, only $t < 200$s is dominant and critical

491   for the analyses of dimensionless time and penetration zone. Thus, we take

492   200s and use helium to calculate the dimensionless time. Another critical

493   parameter to assure enough decay data is the sample diameter greater than 2

494   mm. Thus, we only show the dimensionless time versus porosity for sample

495   diameter greater than 2 mm.

496   Fig. 9 demonstrates that the sample permeability has dominant control on

497   the early- or late-solution selection, and we decipher a concise criterial for

498   three solutions selection. We classify the dimensionless time versus porosity

499   relationship into three cases. Firstly, among the curves shown in Fig. 9, only

500   that corresponding to $k = 0.1$ nD and sample diameter of 2 mm stays below

501   the dashed line representing $\tau = 0.024$. Therefore, the early time solution is

502   appropriate for tight samples with permeabilities less than 0.1 nD (as shown

503   in the analyses of Section 4.3, which also conforms to the situation of the

504   molecular sieve sample that we tested in SI3). Secondly, for permeabilities

505   greater than 10 nD (the curve is above the line of $\tau = 0.024$), the new derived

506   late-time solution, Eq. (3B), is recommended as it is more convenient for

507   mathematical   calculation   without   the   consideration   of   transcendental

508   functions. The reason is that the sample cell can be filled as much as possible

509   (~90% of the volume) with samples and solid objects. However, as the tight

510   rock hardly presents a large value of porosity, the small K_c value is difficult

511   to be achieved with an inconsequential influence between Eq. (3B) and Eq.

512   (3A). Lastly, in the case of permeability around 1 nD, the value of porosity

513   would be critical in the selection of the early- or late-time solutions, as shown

514   in Fig. 9.
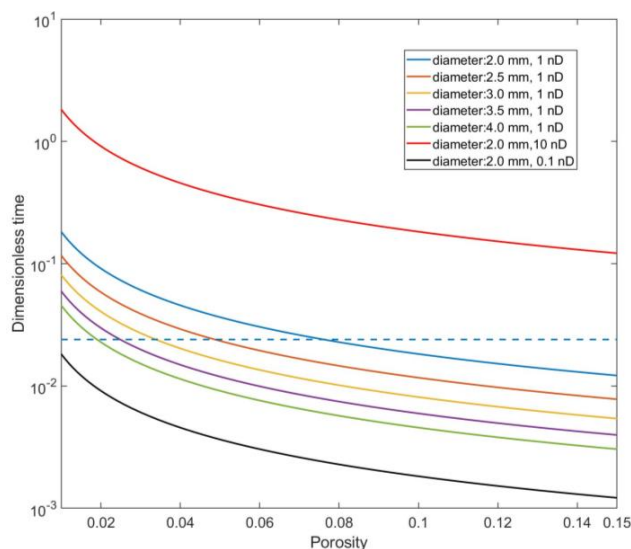
515

516   Fig. 9. Holistic GPT to explore the appropriate solution based on diameter,

517   permeability, and porosity of samples. The legend shows the diameter of granular

518   sample and permeability, along with a dashed line for dimensionless time of 0.024,

519   while regions above and below this value fit for the late- and early-time solutions,

520   respectively.

521   **5. Conclusions**

522   In the present work, we solved fluid flow state equation in granular porous

31

523   media and provided three exact mathematical solutions along with their

524   approximate ones for practical applications of low permeability measurements.

525   The mathematical solutions for the transport coefficient in the GPT were

526   derived for a spherical coordinate system, applicable from laminar flow to

527   slippage-corrected Fickian diffusion. Among the three derivations, one was

528   early-time solution valid when gas storage capacity K_c approaches infinity

529   and two were late-time solutions valid when either K_c is small or K_c tends

530   to infinity. We evaluated the derived solutions for a systematic measurement

531   of extra-low permeabilities in granular media and crushed rocks using

532   experimental methodologies with the data processing procedures. We

533   determined the error for each solution by comparing with the exact solutions

534   presented in the SI. The applicable conditions for such solutions of the GPT

535   were investigated, and we provided the selection strategies for three

536   approximate solutions based the range of sample permeability. In addition, a

537   detailed utilization of GTP was given to build up the confidence in the GPT

538   method through the molecular sieve sample, as it enables a rapid permeability

539   test for ultra-tight rock samples in just tens to hundreds of seconds, with good

540   repeatability.

541   **Data availability.** This work did not use any data from previously published

542   sources, and our experimental data & processing codes of MATLAB are

543   available   at   https://doi.org/10.18738/T8/YZJS7Y,   managed   by   Mavs

544   Dataverse of the University of Texas at Arlington.

545   **Supplement.** An early-version preprint of this work appears as DOI:

546   10.1002/essoar.10506690.2 (Zhang et al., 2021).

547   **Author contributions**. TZ and QHH planned and designed the research,

548   performed the analyses, and wrote the paper with contributions from all co-

549   authors. BG, DK, and ZM participated in the research and edited the paper.

550   **Competing interest.** We declare that we do not have any commercial or

551   associative interest that represents a conflict of interest in connection with the

552   work submitted.

559

560   **Nomenclature**

561   B_{ij} Correction parameter for viscosity, constant

562   c_t Fluid compressibility, Pa^{-1}

563   D Diffusion coefficient, m^2/s

564   F_f Uptake rate of gas outside the sample, dimensionless

565   F_s Uptake rate in the sample, dimensionless

566   f_1 Intercept of Eq. (S40), constant

567   J Physical flux, unit for certain physical phenomenon

568   K_a Apparent transport coefficient defined as Eq. (S9), m^2/s

569   K_c Ratio of gas storage capacity of the total void volume of the system to
570   the pore (including adsorptive and non-adsorptive transport) volume
571   of the sample, fraction

572   K_f Initial density state of the system, fraction

573   k Permeability, m^2

574   k_s Permeability defined as Eq. (S8), m^2/(pa·s)

575   L Coefficient, unit for certain physical transport phenomenon

576   M Molar mass, kg/kmol

577   M_m Molar mass of the mixed gas, kg/kmol

578        $M_{i,j}$ Molar mass for gas i or j, kg/kmol

579   M_s Total mass of sample, kg

580   N Particle number, constant

581   p Pressure, Pa

582   p_{cm} Virtual critical pressure of mixed gas, Pa

583   p_p Pseudo-pressure from Eq. (S1), Pa/s

584   R_a Particle diameter of sample, m

585   R Universal gas constant, 8.314 J/(mol·K)

586   r Diameter of sample, m

587   s_1 Slope of Eq. (S40), constant

588   s_2 Slope of function $Ln(1 - F_s)$, constant

589   s_3 Slope of function $F_s{}^2$, constant

590   T Temperature, K

591   T_{cm} Virtual critical temperature for mixed gas, K

592   t Time, s

593   U_f Dimensionless density of gas outside the sample, dimensionless

594   U_s Dimensionless density in grain, dimensionless

595   U_∞ Maximum density defined as Eq. (S37), dimensionless

596   V_1 Cell volume in upstream of pulse-decay method, m³

597   V_2 Cell volume in downstream of pulse-decay method, m³

598   V_b Bulk volume of sample, m³

599   V_c Total system void volume except for sample bulk volume, m³

600     $\bar{v}$ Dacian velocity in pore volume of porous media, m/s

601   X Pressure force, Pa

602     $y_{i,j}$ Molar fraction for gas i or j, fraction

603   z Gas deviation (compressibility) factor, constant

604   **Greek Letters:**

605   α_n The nth root of Eq. (S30), constant

606   μ Dynamic viscosity, pa·s or N·s/m²

607     $\mu_{i,j}$ Dynamic viscosity for gas i or j, pa·s or N·s/m²

608   μ_{mix} Dynamic viscosity of mixture gas, pa s or N s/m²

609   μ_p Correction term for the viscosity with pressure, pa s or N s/m²

610   ξ Dimensionless radius of sample, dimensionless

611   ρ Density of fluid, kg/m^3

612   ρ_0 Average gas density on the periphery of sample, kg/m^3

613   ρ_1 Gas density in reference cell, kg/m^3

614   ρ_2 Gas density in sample cell, kg/m^3

615   ρ_b Average bulk density for each particle, kg/m^3

616   ρ_f Density of gas changing with time outside sample, kg·m^{-3}·s^{-1}

617     $\rho_{f\infty}$ Maximum value of ρ_f defined as Eq. (S38), kg·m^{-3}·s^{-1}

618   ρ_p Pseudo-density from Eq. (S1), kg·m^{-3}·s^{-1}

619   ρ_s Density of gas changing with time in sample, kg·m^{-3}·s^{-1}

620   ρ_{ps} Pseudo-density of gas changing with time in sample, kg·m^{-3}·s^{-1}

621   ρ_{pf} Pseudo-density of gas changing with time outside sample, kg·m^{-3}·s^{-1}

622   ρ_{p2} Initial pseudo-density of gas in sample, kg·m^{-3}·s^{-1}

623   ρ_{p0} Average pseudo-density of gas on sample periphery, kg·m^{-3}·s^{-1}

624   ρ_{rm} Relative density to the mixed gas, kg·m^{-3}·s^{-1}

625   ρ_{sav} Average value of ρ_{sr} defined as Eq. (S47), kg·m^{-3}·s^{-1}

626   ρ_{sr} Average value of pseudo-density of sample changing with diameter,
627   kg·m^{-3}·s^{-1}

628     $\rho_{s\infty}$ Maximum value of ρ_{sr} defined as Eq. (S46), kg·m^{-3}·s^{-1}

629   τ Dimensionless time, dimensionless

630   ϕ Sample porosity, fraction

631   ϕ_f Total porosity ($\phi_f = \phi_a + \phi_b$) occupied by both free and adsorptive
632   fluids, fraction

References:

Abdassah, D., Ershaghi, I., 1986. Triple-porosity systems for representing naturally fractured reservoirs. SPE Formation Evaluation 1(02), 113-127.

Bibby, R., 1981. Mass transport of solutes in dual‐porosity media. Water Resour. Res. 17(4), 1075-1081.

Bock, H., Dehandschutter, B., Martin, C.D., Mazurek, M., De Haller, A., Skoczylas, F., Davy, C., 2010. Self-sealing of fractures in argillaceous formations in the context of geological disposal of radioactive waste.

Brace, W.F., Walsh, J.B., Frangos, W.T., 1968. Permeability of granite under high pressure. Journal of Geophysical Research 73(6), 2225-2236.

Busch, A., Alles, S., Gensterblum, Y., Prinz, D., Dewhurst, D.N., Raven, M.D., Stanjek, H., Krooss, B.M., 2008. Carbon dioxide storage potential of shales. Int. J. Greenh. Gas Con. 2(3), 297-308.

Carslaw, H.S., Jaeger, J.C., 1959. Conduction of heat in solids.

Chen, X., Pfender, E., 1983. Effect of the Knudsen number on heat transfer to a particle immersed into a thermal plasma. Plasma Chem. Plasma P. 3(1), 97-113.

Civan, F., Devegowda, D., Sigal, R.F., 2013. Critical evaluation and improvement of methods for determination of matrix permeability of shale, Society of Petroleum Engineers.

Cui, X., Bustin, A., Bustin, R.M., 2009. Measurements of gas permeability and diffusivity of tight reservoir rocks: different approaches and their applications. Geofluids 9(3), 208-223.

Devegowda, D., 2015. Comparison of shale permeability to gas determined by pressure-pulse transmission testing of core plugs and crushed samples, Unconventional Resources Technology Conference (URTEC).

Egermann, P., Lenormand, R., Longeron, D.G., Zarcone, C., 2005. A fast and direct method of permeability measurements on drill cuttings. Spe Reserv. Eval. Eng. 8(04), 269-275.

Fakher, S., Abdelaal, H., Elgahawy, Y., El-Tonbary, A., 2020. A Review of Long-Term Carbon Dioxide Storage in Shale Reservoirs, OnePetro.

Gensterblum, Y., Ghanizadeh, A., Cuss, R.J., Amann-Hildenbrand, A., Krooss, B.M., Clarkson, C.R., Harrington, J.F., Zoback, M.D., 2015. Gas transport and storage capacity in shale gas reservoirs – A review. Part A: Transport processes. Journal of Unconventional Oil and Gas Resources 12, 87-122.

Ghanbarian, B., 2022a. Estimating the scale dependence of permeability at pore and core scales: Incorporating effects of porosity and finite size. Adv. Water Resour. 161, 104123.

Ghanbarian, B., 2022b. Scale dependence of tortuosity and diffusion: Finite-size scaling analysis. J. Contam. Hydrol. 245, 103953.

681 Ghanbarian, B., Hunt, A.G., Daigle, H., 2016. Fluid flow in porous media with rough pore‐
682   solid interface. Water Resour. Res. 52(3), 2045-2058.

683 Guidry, K., Luffel, D., Curtis, J., 1996. Development of laboratory and petrophysical
684   techniques for evaluating shale reservoirs. Final technical report, October 1986-
685   September 1993, ResTech Houston, Inc., TX (United States).

686 Gutierrez, M., Øino, L.E., Nygaard, R., 2000. Stress-dependent permeability of a de-
687   mineralised fracture in shale. Mar. Petrol. Geol. 17(8), 895-907.

688 Haggerty, R., Gorelick, S.M., 1995. Multiple‐rate mass transfer for modeling diffusion and
689   surface reactions in media with pore‐scale heterogeneity. Water Resour. Res. 31(10),
690   2383-2400.

691 Haskett, S.E., Narahara, G.M., Holditch, S.A., 1988. A method for simultaneous
692   determination of permeability and porosity in low-permeability cores. SPE formation
693   evaluation 3(03), 651-658.

694 Haszeldine, S., Lu, J., Wilkinson, M., Macleod, G., 2006. Long-timescale interaction of CO2
695   storage with reservoir and seal: Miller and Brae natural analogue fields North Sea.
696   Greenhouse Gas Control Technology 8.

697 Heller, R., Vermylen, J., Zoback, M., 2014. Experimental investigation of matrix permeability
698   of gas shalesExperimental Investigation of Matrix Permeability of Gas Shales. Aapg Bull.
699   98(5), 975-995.

700 Hu, Q., Ewing, R.P., Dultz, S., 2012. Low pore connectivity in natural rock. J. Contam. Hydrol.
701   133, 76-83.

702 Hu, Q., Ewing, R.P., Rowe, H.D., 2015. Low nanopore connectivity limits gas production in
703   Barnett formation. Journal of Geophysical Research: Solid Earth 120(12), 8073-8087.

704 Huenges, E., 2016., pp. 743-761, Elsevier.

705 Javadpour, F., 2009. Nanopores and apparent permeability of gas flow in mudrocks (shales
706   and siltstone). Journal of Canadian Petroleum Technology 48(08), 16-21.

707 Jia, B., Tsau, J., Barati, R., Zhang, F., 2019. Impact of Heterogeneity on the Transient Gas
708   Flow Process in Tight Rock. Energies 12(18), 3559.

709 Kamath, J., 1992. Evaluation of accuracy of estimating air permeability from mercury-
710   injection data. SPE Formation evaluation 7(04), 304-310.

711 Khosrokhavar, R., 2016. Shale gas formations and their potential for carbon storage:
712   opportunities and outlook. Mechanisms for CO2 Sequestration in Geological Formations
713   and Enhanced Gas Recovery, 67-86.

714 Kim, C., Jang, H., Lee, J., 2015. Experimental investigation on the characteristics of gas
715   diffusion in shale gas reservoir using porosity and permeability of nanopore scale. J. Petrol.
716   Sci. Eng. 133, 226-237.

717   Kim, J., Kwon, S., Sanchez, M., Cho, G., 2011. Geological storage of high level nuclear waste.
718   Ksce J. Civ. Eng. 15(4), 721-737.
719   Liu, W., Li, Y., Yang, C., Daemen, J.J., Yang, Y., Zhang, G., 2015. Permeability
720   characteristics of mudstone cap rock and interlayers in bedded salt formations and
721   tightness assessment for underground gas storage caverns. Eng. Geol. 193, 212-223.
722   Lu, J., Wilkinson, M., Haszeldine, R.S., Fallick, A.E., 2009. Long-term performance of a
723   mudrock seal in natural CO2 storage. Geology 37(1), 35-38.
724   Luffel, D.L., Hopkins, C.W., Schettler Jr, P.D., 1993. Matrix permeability measurement of
725   gas productive shales, Society of Petroleum Engineers.
726   Neuzil, C.E., 1986. Groundwater flow in low‐permeability environments. Water Resour.
727   Res. 22(8), 1163-1195.
728   Neuzil, C.E., 2013. Can shale safely host US nuclear waste? Eos, Transactions American
729   Geophysical Union 94(30), 261-262.
730   Peng, S., Loucks, B., 2016. Permeability measurements in mudrocks using gas-expansion
731   methods on plug and crushed-rock samples. Mar. Petrol. Geol. 73, 299-310.
732   Pini, R., 2014. Assessing the adsorption properties of mudrocks for CO2 sequestration.
733   Energy Procedia 63, 5556-5561.
734   Profice, S., Lasseux, D., Jannot, Y., Jebara, N., Hamon, G., 2012. Permeability, porosity and
735   klinkenberg coefficien determination on crushed porous media. Petrophysics 53(06), 430-
736   438.
737   Rasmuson, A., 1985. The effect of particles of variable size, shape and properties on the
738   dynamics of fixed beds. Chem. Eng. Sci. 40(4), 621-629.
739   Roy, S., Raju, R., Chuang, H.F., Cruden, B.A., Meyyappan, M., 2003. Modeling gas flow
740   through microchannels and nanopores. J. Appl. Phys. 93(8), 4870-4879.
741   Ruthven, D.M., 1984. Principles of adsorption and adsorption processes, John Wiley & Sons.
742   Ruthven, D.M., Loughlin, K.F., 1971. The effect of crystallite shape and size distribution on
743   diffusion measurements in molecular sieves. Chem. Eng. Sci. 26(5), 577-584.
744   Tarkowski, R., 2019. Underground hydrogen storage: Characteristics and prospects.
745   Renewable and Sustainable Energy Reviews 105, 86-94.
746   Wu, T., Zhang, D., Li, X., 2020. A radial differential pressure decay method with micro-plug
747   samples for determining the apparent permeability of shale matrix. J. Nat. Gas Sci. Eng.
748   74, 103126.
749   Yang, M., Annable, M.D., Jawitz, J.W., 2015. Back diffusion from thin low permeability
750   zones. Environ. Sci. Technol. 49(1), 415-422.

751 Zhang, J.J., Liu, H., Boudjatit, M., 2020. Matrix permeability measurement from fractured
752   unconventional source-rock samples: Method and application. J. Contam. Hydrol.,
753   103663.
754 Zhang, T., Hu, Q., Chen, W., Gao, Y., Feng, X., Wang, G., 2021. Analyses of True-Triaxial
755   Hydraulic Fracturing of Granite Samples for an Enhanced Geothermal System.
756   Lithosphere-Us 2021(Special 5).
757 Zhang, T., Zhou, W., Hu, Q., Xu, H., Zhao, J., Zhang, C., 2021. A pulse-decay method for
758   low permeability analyses of granular porous media: Mathematical solutions and
759   experimental methodologies.
760

761